Structure–Property–Fracture Mechanism Correlation in Heat-Affected Zone of X100 Ferrite–Bainite Pipeline Steel

XUEDA LI, XIAOPING MA, S.V. SUBRAMANIAN, R.D.K. MISRA, and CHENGJIA SHANG

Structural performance of a weld joint primarily depends on the microstructural characteristics of heat-affected zone (HAZ). In this regard, the HAZ in X100 ferrite–bainite pipeline steel was studied by separating the HAZ into intercritically reheated coarse-grained (ICCG) HAZ containing and non-containing regions. These two regions were individually evaluated for Charpy impact toughness and characterized by electron back-scattered diffraction (EBSD). Low toughness of ~50 J was obtained when the notch of impact specimen encountered ICCGHAZ and high toughness of ~180 J when the notch did not contain ICCGHAZ. Fracture surface was ~60 pct brittle in the absence of ICCGHAZ, and 95 pct brittle (excluding shear lip) in the presence of ICCGHAZ in the impact tested samples. The underlying reason is the microstructure of ICCGHAZ consisted of granular bainite and upper bainite with necklace-type martensite–austenite (M–A) constituent along grain boundaries. The presence of necklace-type M-A constituent notably increases the susceptibility of cleavage microcrack nucleation. ICCGHAZ was found to be both the initiation site of the whole fracture and cleavage facet initiation site during brittle fracture propagation stage. Furthermore, the study of secondary microcracks beneath CGHAZ and ICCGHAZ through EBSD suggested that the fracture mechanism changes from nucleation-controlled in CGHAZ to propagation-controlled in ICCGHAZ because of the presence of necklace-type M-A constituent in ICCGHAZ. Both fracture mechanisms contribute to the poor toughness of the sample contained ICCGHAZ.

DOI: 10.1007/s40553-014-0036-3
© ASM International (ASM) and The Minerals, Metals, & Materials Society (TMS) 2015

I. INTRODUCTION

THERMO-MECHANICALLY processed X80-X100 pipeline steels with ferrite and bainite microstructure have good combination of strength, toughness, and ductility.[1,2] However, welding of pipeline steels continues to be a cause for concern because of the presence of local brittle zone (LBZ) in the heat-affected zone (HAZ).[3,4] During deformation, cleavage fracture can nucleate at the LBZ[5,6] and subsequently propagate from LBZ. In the HAZ, there are several sub-zones including coarse-grained (CG) HAZ, fine-grained (FG) HAZ, intercritically reheated coarse-grained (ICCG) HAZ and so on. Different microstructures are obtained in these sub-zones because they experienced different thermal history during the welding process. Extensive studies on microstructure property correlation in HAZ were done in the past few decades. It is generally accepted that CGHAZ and ICCGHAZ are the most detrimental regions from the point of view of toughness and cleavage fracture may occur in the two regions during impact.[3,5–8] Thus, there is a need to understand the correlation of structure–property–cleavage fracture mechanism in the HAZ, especially in CGHAZ and ICCGHAZ.

In cleavage fracture, both nucleation and propagation of cleavage cracks govern the ultimate absorbed energy. A number of models or mechanisms have been proposed to describe crack nucleation and propagation. In regard to nucleation, at least three possible mechanisms have been suggested and include: (a) crack initiation at grain boundaries caused by pile-up of dislocations,[9,10] (b) cracking of inclusions, large second phase particle or martensite–austenite (M–A) constituent present within the grains or along the grain boundaries,[5–7, 11], and (c) decohesion of inclusions/M–A from matrix.[6–8] Cleavage fracture occurs when (1) the maximum principal stress (σ_{yy}) close to the crack tip exceeds fracture stress (σ_f) over a characteristic distance,[12] or (2) the microcracks, nucleated ahead of the main crack tip because of high stress field,[13] interconnect with each other.[14] During propagation, there is competition between the microcracks formed at the crack front. The main crack selects the most convenient approach for propagation (weakest link theory[15]), such that the secondary microcracks are left underneath the fracture surface of the main crack.

To develop comprehensive understanding of the mechanism of nucleation and propagation of a cleavage fracture, it is important that, in addition to the

XUEDA LI, Ph.D. Candidate, and CHENGJIA SHANG, Professor, are with the School of Material Science and Engineering, University of Science and Technology Beijing, Beijing 100083, P.R. China. Contact e-mail: cjshang@ustb.edu.cn XIAOPING MA, Post Doctor, and S.V. SUBRAMANIAN, Professor, are with the Department of Material Science and Engineering, McMaster University, Hamilton, L8S 4L8, Canada. R.D.K. MISRA, Professor, is with the Department of Metallurgical and Materials Engineering, University of Texas at El Paso, El Paso, TX, 79968.

Manuscript submitted July 14, 2014.
Article published online January 13, 2015

examination of the fracture surface, fundamental insight is obtained from the cleavage cracks. In this regard, electron back-scattered diffraction (EBSD) is an appropriate technique that provides crystallographic information of the cleavage cracks.[14] Main crack is generally difficult to characterize using EBSD primarily because of poor indexing rate introduced by the high strain and large residual stress after the destructive Charpy v-notch impact test. However, secondary microcracks that are nucleated at the crack tip and are retarded or arrested by the high angle boundary (HAB), small grains (packets) or in some instances M−A constituent[7] can provide information on crack nucleation and propagation process. Recently, a few studies on the characterization of brittle cracks using EBSD have been reported.[14,16–20] However, initiation and propagation of cleavage cracks in the HAZ of high strength (*e.g.* X100) have not been explored to the best of our understanding. In the present study, secondary microcracks in the HAZ of X100 pipeline steel longitudinal submerged arc welding (LSAW) real weld were studied *via* EBSD, and the mechanism of cleavage fracture nucleation and propagation is discussed.

II. EXPERIMENTAL

High-strength low-carbon and high-niobium X100 pipeline steel was produced by thermo-mechanical control process (TMCP). Chemical composition of X100 was listed in Table I. The plate with gage thickness of 14.7 mm was made into pipes of 1219 mm outer diameter (OD) using U-forming, O-forming, and mechanical expanding (UOE) process. Double-pass LSAW with preheat temperature of 353 K (80 °C) was applied during welding. The inter-pass temperature was 393 K (120 °C). Detailed welding parameters were listed in Table II. Four wires were tandem arranged and welded simultaneously. The main reason why four wires were applied is to increase the welding speed and productivity. The chemical composition of weld metal was presented in Table I. The weld joint was cut from the as-welded pipe (geometry presented in Figure 1(a)) for the experimental study. Macrograph of the weld joint was presented in Figure 1(b). Microstructure of the HAZ was characterized using light microscope (LM, Zeiss Stereo Microscopy), scanning electron microscope (SEM, JEOL-JSM7000F), EBSD (Oxford Synergy system), and transmission electron microscopy (TEM, Philips CM12). Charpy impact samples were machined transverse to the weld seam according to Figure 1(a). Instrumented Charpy impact v-notch test (IMP450 J Dynatup, Instron) was carried out at 253 K (−20 °C) with the notch located at different positions in the HAZ (Notch I and II) as illustrated in Figure 1(c). The side of each sample was etched to exactly locate the notch position. Four samples were examined for each notch position. The fracture surface of the Charpy impact sample was observed by LM and SEM.

In order to study the secondary microcracks beneath the fracture surface, the fracture sample with notch II was cut along the red line 1 (Figures 1(c) through (d)) which encountered the CGHAZ region of the first pass. The EBSD sample was shown in Figure 1(e). To prevent the edge effect, prior to grinding and polishing, the sample was mounted in epoxy containing some nickel powder to improve the strength and electrical conductivity of the epoxy mount. The intersection surface (plane 1 in Figures 1(c) through (d)) was ground and mechanically polished with 50 nm colloidal silica. Number of microcracks beneath the whole fracture route was counted using LM. Then the mounted sample was sputter coated with 3 nm thick layer of carbon to avoid charging during EBSD scanning. The first EBSD map showing secondary microcracks in CGHAZ was obtained at plane 1. After EBSD scanning, the carbon layer was wiped out and the surface was etched with 4 pct nital. *In situ* optical micrograph of EBSD scanning

Table I. Chemistry of X100 Ferrite−Bainite Pipeline Steel and Weld Metal

Content (wt pct)	C	Si	Mn	Nb	Cr	Mo	Ni	Ti	N
X100	0.07	0.25	1.94	0.081	0.26	0.24	0.17	0.015	0.004
Weld metal	0.06	0.33	1.81	0.046	0.18	0.28	0.11	0.022	0.007

Table II. Welding Parameters of Dual-Pass LSAW

Pass	Welding Method	Wire no.	Current (mA)	Voltage (V)	Polarity	Speed (m/min)	Heat Input (kJ/cm)
Pre-weld	Gas shielded	/	850	24	DC-RP	3.5	4.1
Innerside	LSAW	1	850	32	DC-RP	1.75	32.8
		2	700	38	AC		
		3	550	40	AC		
		4	500	40	AC		
Outside	LSAW	1	950	32	DC-RP	1.80	33.9
		2	750	38	AC		
		3	550	40	AC		
		4	500	42	AC		

DC: direct current; AC: alternate current; RP: reversed polarity.

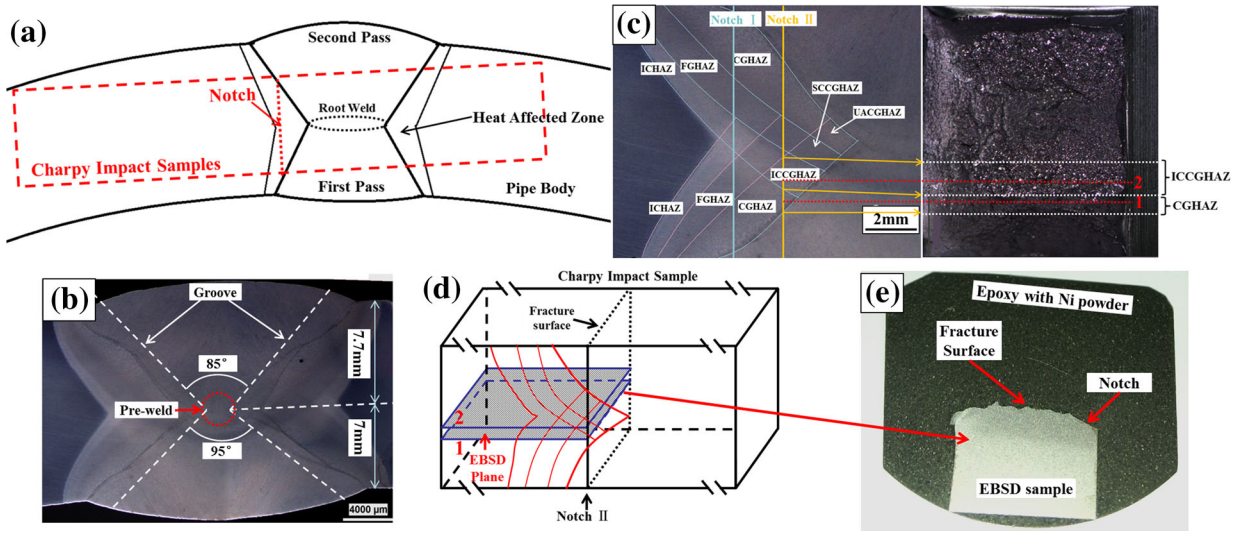

Fig. 1—(*a*) Schematic of weld geometry and Charpy impact sample orientation; (*b*) Macrograph of LSAW weld joint; (*c*) Notch position and EBSD map position (FGHAZ: fine-grained HAZ; ICHAZ: intercritically reheated HAZ, SCCGHAZ: supercritically reheated CGHAZ; UACGHAZ: unaltered CGHAZ); (*d*) Schematic showing how EBSD samples were sectioned; (*e*) EBSD sample mounted in epoxy.

area was obtained. Next, the sample surface was further ground by ~800 μm into ICCGHAZ region (plane 2 in Figures 1(c) through (d)), and the second EBSD map was recorded using the same procedure described above. EBSD data was analyzed using HKL software.

III. RESULTS AND DISCUSSION

A. *Microstructure*

The microstructure of X100 pipeline steel was presented in Figure 2. X100 is a well-designed ferrite–bainite microstructure. Band slope map* (Figure 2(a)) clearly shows the dual phase microstructure of X100. Fine polygonal ferrite grains (with average size of ~5 μm) distribute along pancaked prior austenite grain boundaries. Fraction of ferrite is 31 pct. Bainite with high density of HAB is located in between ferrite. In this type of microstructure, ferrite acts as a soft phase which deforms first in the deformation process and contributes to high uniform elongation and low strain aging sensitivity. Bainite acts as a hard phase which contributes to high tensile strength. Therefore, dual phase X100 has excellent mechanical properties, such as large uniform elongation, low yield ratio, low strain aging sensitivity, and good toughness. Detailed discussion about microstructure property of X100 was reported in Reference 2. Toughness of X100 base plate is listed in Table III.

In the HAZ, microstructure of base plate was erased due to the heat affect of welding process. The microstructure of CGHAZ and ICCGHAZ are presented in Figure 3. In CGHAZ, the base plate was affected by single thermal cycle with peak temperature of ~1623 K (1350 °C) and slow cooling rate of ~6 K/s (6 °C/s). Therefore, the grains in CGHAZ were coarse with average grain size of ~80 μm, and the microstructure was primarily consisted of granular bainite and upper bainite (Figures 3(a) through (b)). Grain boundaries in CGHAZ were clean, without the presence of M–A constituent.

ICCGHAZ is the region where CGHAZ was reheated to the intercritical region (Ac_1-Ac_3). Part of the matrix reverted to austenite and prior austenite grain boundary was the preferred nucleation site for reverted structure. Therefore, the matrix microstructure of ICCGHAZ (Figures 3(c) through (d)) still primarily comprised of upper bainite, granular bainite, and a small fraction of acicular ferrite. Between upper bainite laths, thin M–A film was noted in some regions, Figure 3(e). During cooling stage, the reverted austenite transformed into bainite and M–A constituent.[21] Thus, continuous and necklace-type M–A constituent was present along the coarse prior austenite grain boundaries.

EBSD all-Euler map indicated that the density of HAB is very low both in the CGHAZ and ICCGHAZ (Figures 3(b), (d)). Low density of HAB is not effective in retarding or arresting the brittle cracks.[22] Thus, critical Griffith crack length is easily satisfied and catastrophic failure occurs.

SEM and TEM characterization of M–A constituent were presented in Figures 3(e) through (f). It is interesting that, as shown in Figure 3(f), layer-by-layer (dark–bright–dark) structure was frequently observed within M–A constituent. The layer-by-layer structure was also characterized in EBSD all-Euler map (Figure 3(d)). It is likely to be the martensite–austenite layer-by-layer structure. Detailed structure within M–A constituent and phase transformation mechanism of M–A constituent were rarely studied in the previous research. In-depth characterization and study about this structure is one of interests in our future research.

*Band slope is an image quality factor derived from the Hough transformation which is describing the maximum intensity gradient at the margins of the Kikuchi bands in an EBSP (Electron Back-scattered Patterns).

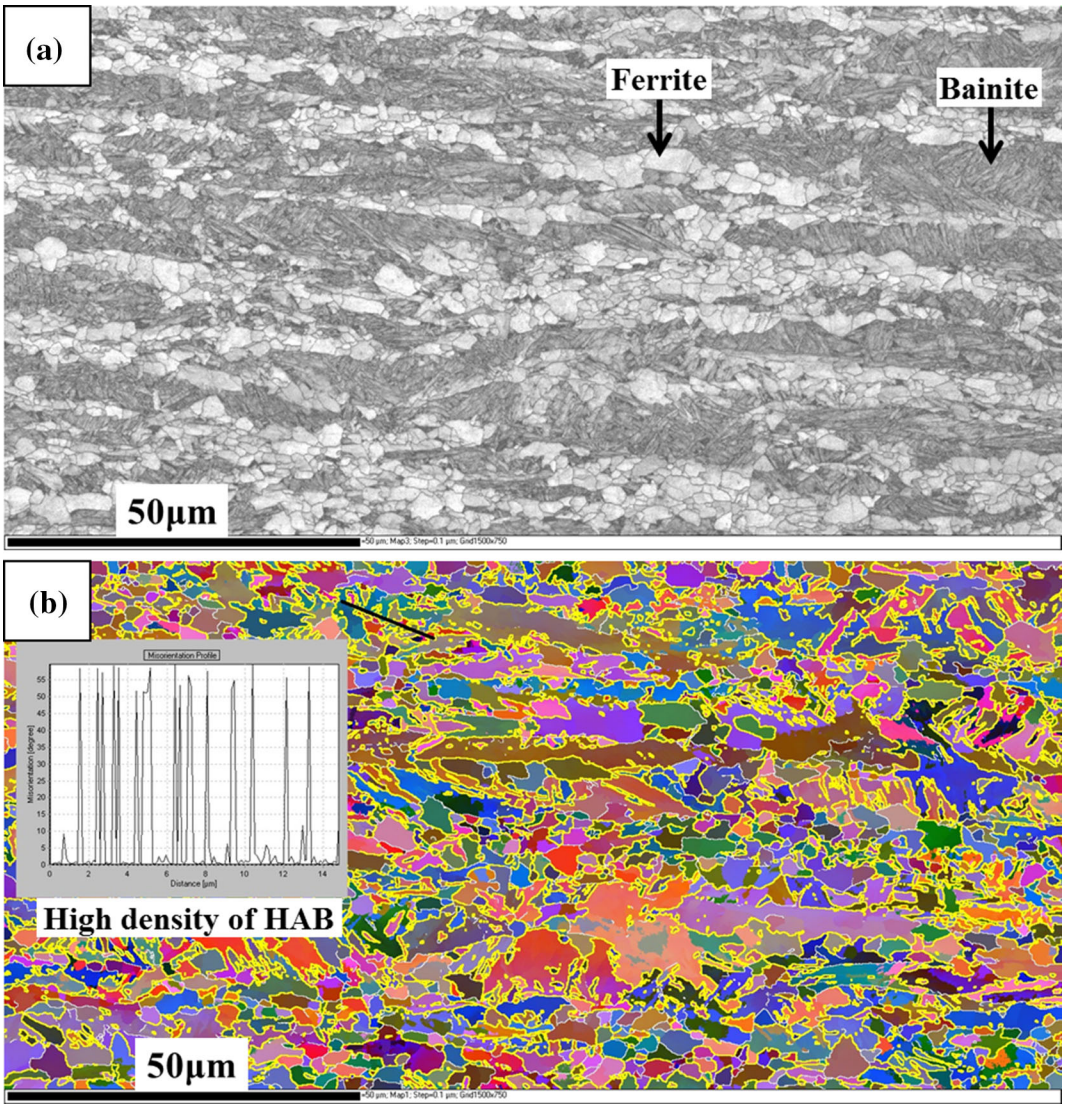

Fig. 2—EBSD characterization of X100 ferrite−bainite pipeline steel. (*a*) Band slope map; (*b*) All-Euler map and density of HAB diagram (yellow line represents >45 deg grain boundary).

Table III. Charpy Impact Energy of Base Plate, Samples with Notch I, II, and Weld Metal at 253 K (−20 °C)

	Charpy Impact Energy (J)				
Position	Single				Average
Base plate	255	228	254	268	215
Notch I	211	174	229	119	183
Notch II	38	51	64	50	51
Weld metal	87	82	78	80	82

The size of M-A constituent in ICCGHAZ was calculated by averaging 30 particles in TEM graphs. Majority of M−A constituent was approximately elliptical and was ~2 μm in length and ~1 μm in thickness. This kind of M−A constituent can promote nucleation of brittle fracture either through cracking or debonding from the matrix.[5–7]

B. *Charpy Impact Toughness and Fracture Surface Characterization*

Charpy impact energy of X100 base plate, samples with notch I, II, and weld metal at −20 °C is presented in Table III. The average Charpy impact energy of notch I was 183 J and is ~3.6 times that of notch II

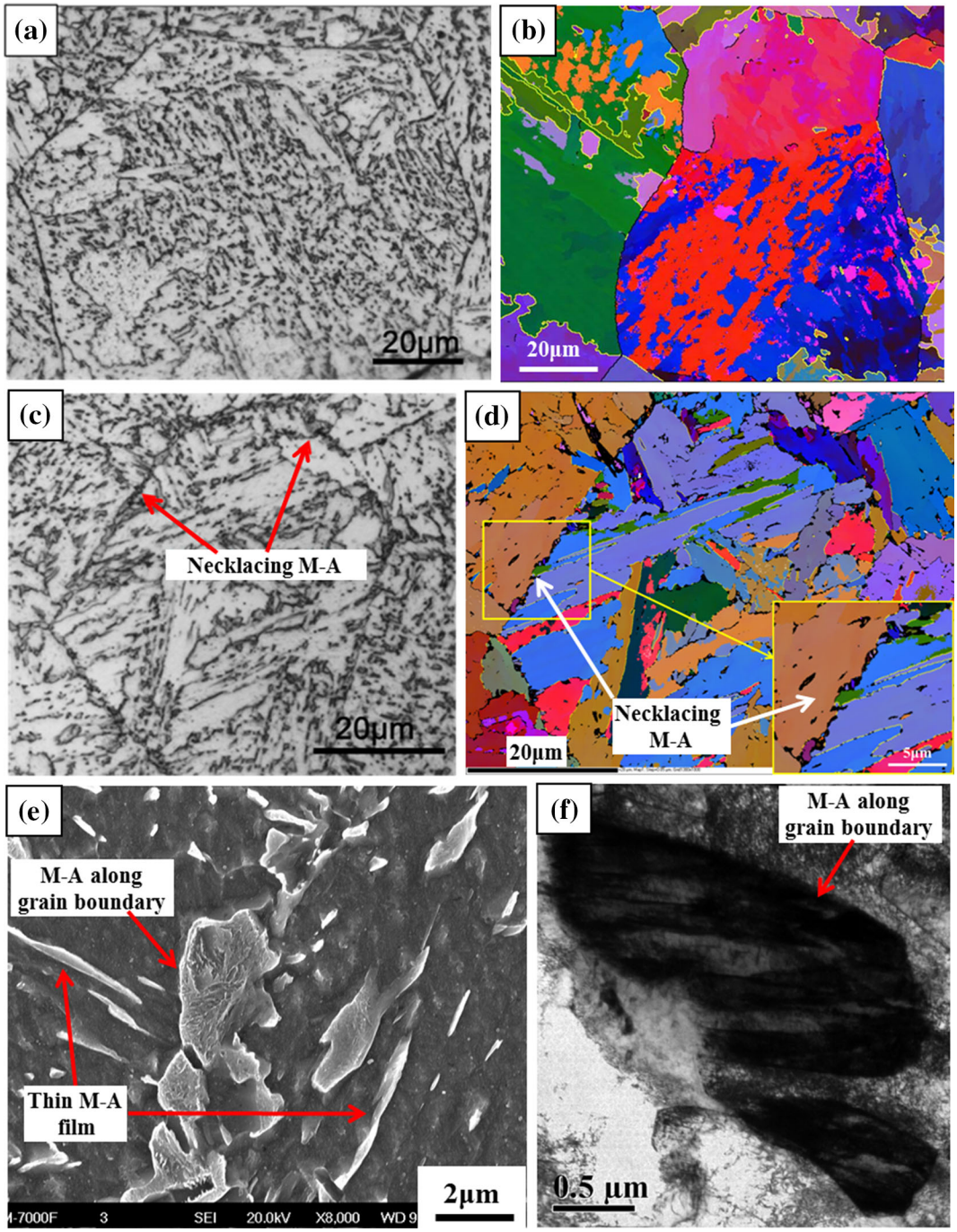

Fig. 3—(*a*) and (*b*) Microstructure of CGHAZ; (*c*) and (*d*) Microstructure of ICCGHAZ; (*e*) and (*f*) SEM and TEM characterization of M-A constituent along grain boundary in ICCGHAZ (In EBSD map, yellow line represents >45 deg grain boundary, black line represents 15-45 deg grain boundary).

(51 J). Significant difference in impact energy between notch I and II is because they encountered different sub-zones of the weld joint, as presented in Figure 1(c). In notch I, CGHAZ, FGHAZ, and ICHAZ regions were present, while in notch II, fusion zone, CGHAZ, ICCGHAZ, and overlapped FGHAZ regions were present. Charpy impact energy is the average of these sub-zones, but is dominated by the most brittle part. An important difference between notch I and II is the presence of ICCGHAZ in notch II. Low toughness of sample with notch II is unlikely to be associated with the fusion zone because the average Charpy impact energy of fusion zone was 82 J and is 1.6 times of sample with notch II. Thus, ICCGHAZ is the most detrimental region and is responsible for low toughness of the sample with notch II.

The fracture surface and instrumented Charpy impact curves recorded for sample with notch I and II are presented in Figure 4. The fracture surface was ~40 pct

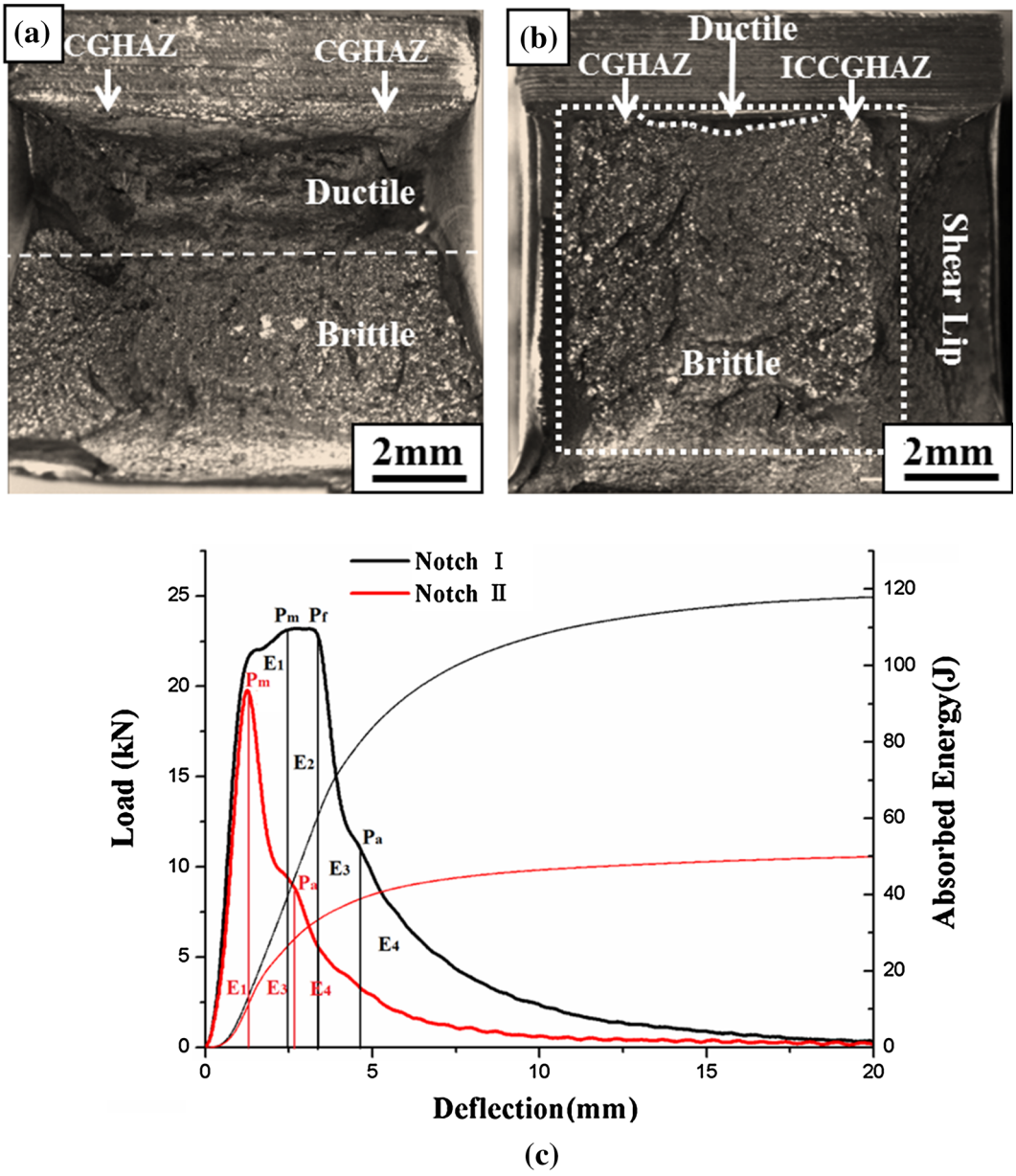

(c)

Fig. 4—The fracture surfaces of sample with notch I (*a*) and II (*b*) and instrumented Charpy impact curves (*c*). (E_1-crack initiation energy, E_2-crack propagation energy, E_3-energy absorbed during brittle fracture, E_4-post brittle fracture energy, P_m-maximum impact load, P_f-brittle fracture start load, P_a-brittle fracture arrested load).

ductile and ~60 pct brittle associated with sample with notch I. In the sample with notch II, there existed a shear lip on the right which was characterized as ductile dimples. The shear lip was along the fusion line between HAZ and weld metal. The existence of shear lip contributed to the absorbed energy. Otherwise, the absorbed energy would be much less than 50 J. Except the shear lip, the fracture surface is 95 pct brittle. Only 5 pct of ductile fracture underneath the middle part of the notch was characterized. This can be directly related to the impact toughness data presented in Table III. Large fraction of ductile fracture in notch I contributed to high toughness. Instrumented Charpy impact curve indicated that in sample with notch II, catastrophic brittle fracture occurred before the peak load was reached and the stable propagation stage (E_2) was absent. While in the sample with notch I, there was a stable propagation stage (E_2), which was correlated to 40 pct ductile fracture in the fracture surface, prior to the catastrophic brittle fracture.

The fracture behavior was influenced by the local microstructure (Figure 4(b)). Fracture surface of CGHAZ and ICCGHAZ region was brighter than the other regions, which indicated that CGHAZ and ICCGHAZ are more brittle. SEM micrographs of the fracture surface of sample with notch I and II are presented in Figure 5. In the sample with notch II, fracture surface of CGHAZ and ICCGHAZ (Figures 5(c) through (d)) was characterized by transgranular cleavage with large cleavage facets. In the ICCGHAZ region (Figure 5(d)), a

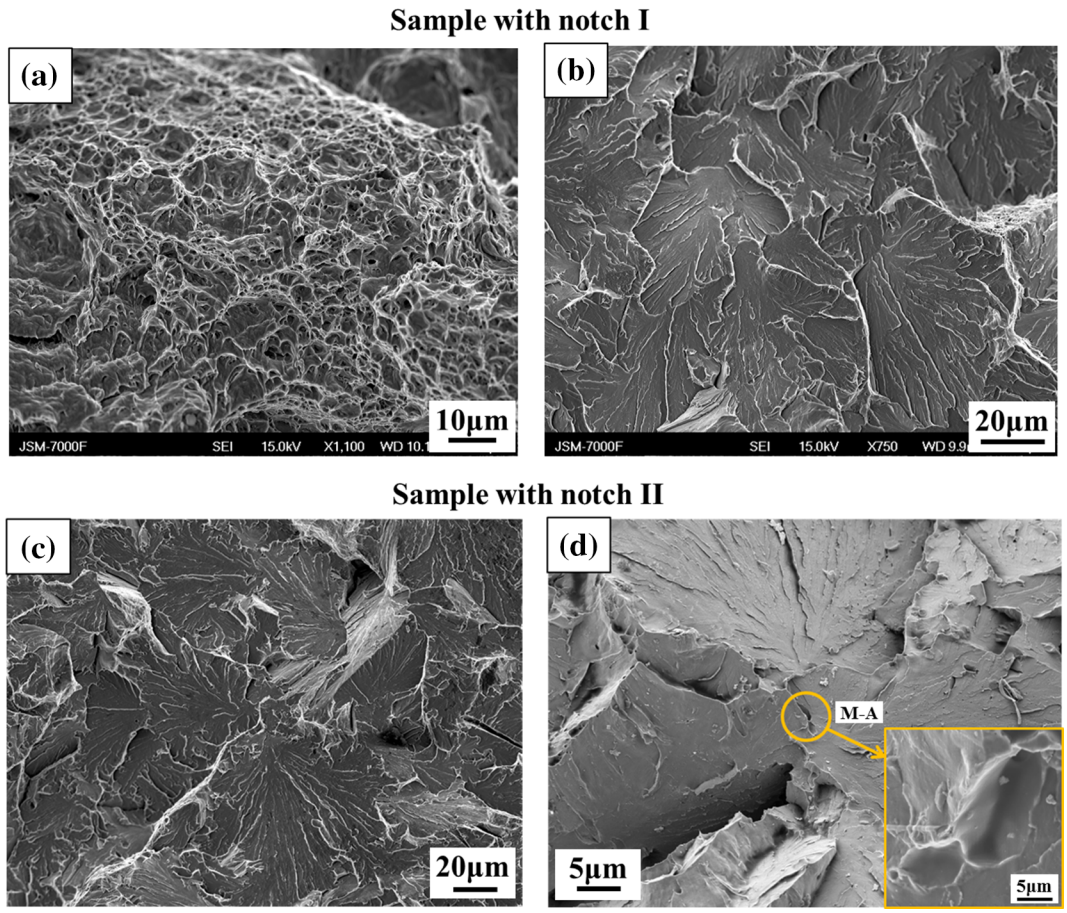

Fig. 5—SEM micrographs of fracture surface of samples with notch I and notch II. (*a*) Ductile fracture; (*b*) Cleavage fracture; (*c*) Cleavage fracture in CGHAZ; (*d*) Cleavage fracture initiated from M−A constituent in ICCGHAZ.

number of cleavage facets initiated from some particles which are most likely to be M-A constituent, because EDS data of these particles showed similar chemical composition to the matrix. But in CGHAZ region (Figure 5(d)), cleavage facets initiated from particles were not found. Therefore, the existence of necklace-type M−A constituent can notably promote the nucleation of brittle crack. Davis *et al.*[5] proposed cleavage fracture initiation mechanisms associated with the M−A constituent. It was proposed that when there is necklace-type M−A constituent, there is ''overlap of transformation-induced residual tensile stresses'' and enhancement of stress concentration due to strength mismatch between M−A and matrix during deformation. Thus, M−A constituent that is presented as a continuous and interconnected structure is detrimental to toughness. In our case, a number of nucleation sites caused by debonding of M-A constituent from the matrix were observed. Similar results were reported by Mohseni *et al.*[6]

Figures 5(a) and (b) presented the ductile and brittle fracture surface in sample with notch I. Notch I encountered large fraction of CGHAZ, but with the absence of ICCGHAZ in notch I, the CGHAZ was characterized by ductile fracture during the first stage of fracture process. This means CGHAZ itself was not very brittle. Only when ICCGHAZ was present, CGHAZ behaved totally brittle. Thus, ICCGHAZ is the dominant factor that controls the fracture behavior and impact energy.

In the sample with notch I, fracture initiation site of the whole sample was found underneath the notch locating at ICCGHAZ area. The SEM characterization of fracture initiation site with different magnifications was presented in Figure 6. Fracture initiation site was 460 μm underneath the notch root. Griffiths *et al.*[13] proposed that ''the distribution of plastic strain around the notch root shows that the surface of the notch root is subject to a relatively constant strain over a distance of about l-2 times the root radius. The distribution of stress within the plastic zone is such that the maximum stress lies on the symmetry axis but at some distance behind the elastic–plastic interface.'' Root radius of Charpy v-notch is 0.25 mm. Therefore, the maximum stress should appear behind 250-500 μm from the notch surface, which is consistent with the result (460 μm) in the present research. Thus, ICCGHAZ can not only be the initiation site of the whole fracture but also be the cleavage facet initiation site during brittle fracture propagation stage. The existence of ICCGHAZ can notably promote brittle fracture and result in low toughness.

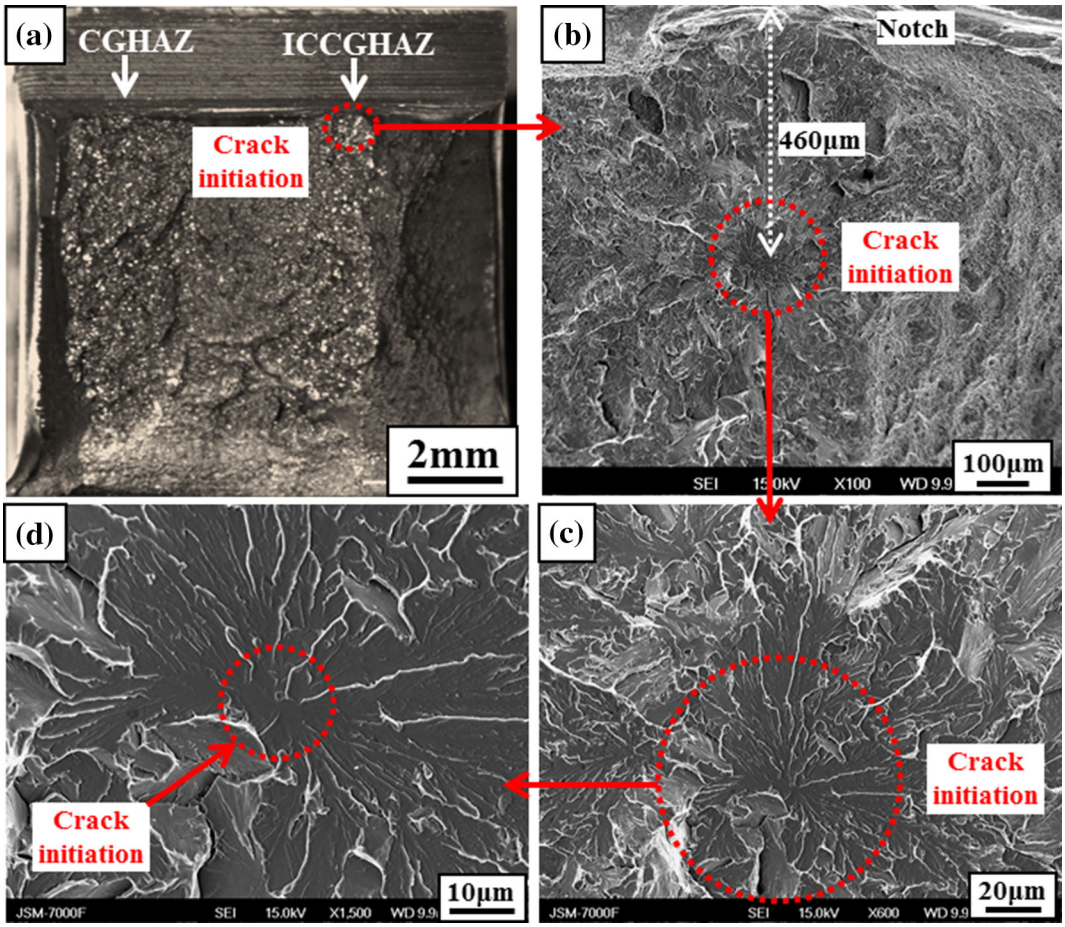

Fig. 6—Characterization of crack initiation site of the whole fracture with different magnifications (*a*) 10 times; (*b*) 100 times; (*c*) 600 times; (*d*) 1500 times.

C. *Secondary Microcracks*

One sample with notch II was sectioned to examine the secondary microcracks beneath the fracture surface according to Figures 1(c) through (e). Characterization of secondary microcracks underneath the brittle fracture surface of CGHAZ (plane 1) and ICCGHAZ (plane 2) are presented in Figures 7 and 8. Whole area beneath the fracture surface of CGHAZ (plane 1) and ICCGHAZ (plane 2) were examined by LM. Number of microcracks in each plane was counted. The results showed that only 9 microcracks were found underneath the CGHAZ fracture surface (plane 1), while 48 microcracks were noted beneath the ICCGHAZ fracture surface (plane 2). Number of secondary microcracks in the ICCGHAZ was much greater than in the CGHAZ. This implies the difference in the susceptibility of secondary microcrack initiation in the two regions. The necklace-type M−A constituent increases stress intensification and provides more nucleation sites for cleavage fracture through cracking of M−A or debonding of M-A from the matrix.[5–7] The difference in the number of secondary microcracks in CGHAZ and ICCGHAZ is indicative of different fracture mechanisms operating in the two regions. In CGHAZ, nucleation of brittle cracks is the critical event: the brittle crack nucleated and immediately propagated, thus only few secondary microcracks were left beneath the fracture surface. This is referred as nucleation-controlled.[9,23] While in ICCGHAZ, fracture mechanism was propagation-controlled[9]: many microcracks nucleated in front of the crack tip, and the fracture proceeded through interconnection of microcracks. Fracture mechanism changes due to the presence of necklace-type M−A constituents in the ICCGHAZ. Both nucleation-controlled and propagation-controlled fracture mechanisms contribute to the poor toughness of ICCGHAZ containing sample. Afterward, another two samples with notch II were sectioned and examined using LM to make sure that the statement above is not based on a lucky section. The trend of number of microcracks in these two samples was similar with the one mentioned above: much more secondary microcracks were found in ICCGHAZ than in CGHAZ.

In Figures 7(a) and 8(a), the propagating direction of the microcracks was altered once they encountered high angle boundaries (HAB, yellow line, >45 deg). Low angle boundaries (LAB, green line, 15 ~ 45 deg) are not believed to be effective in deflecting the microcracks. In

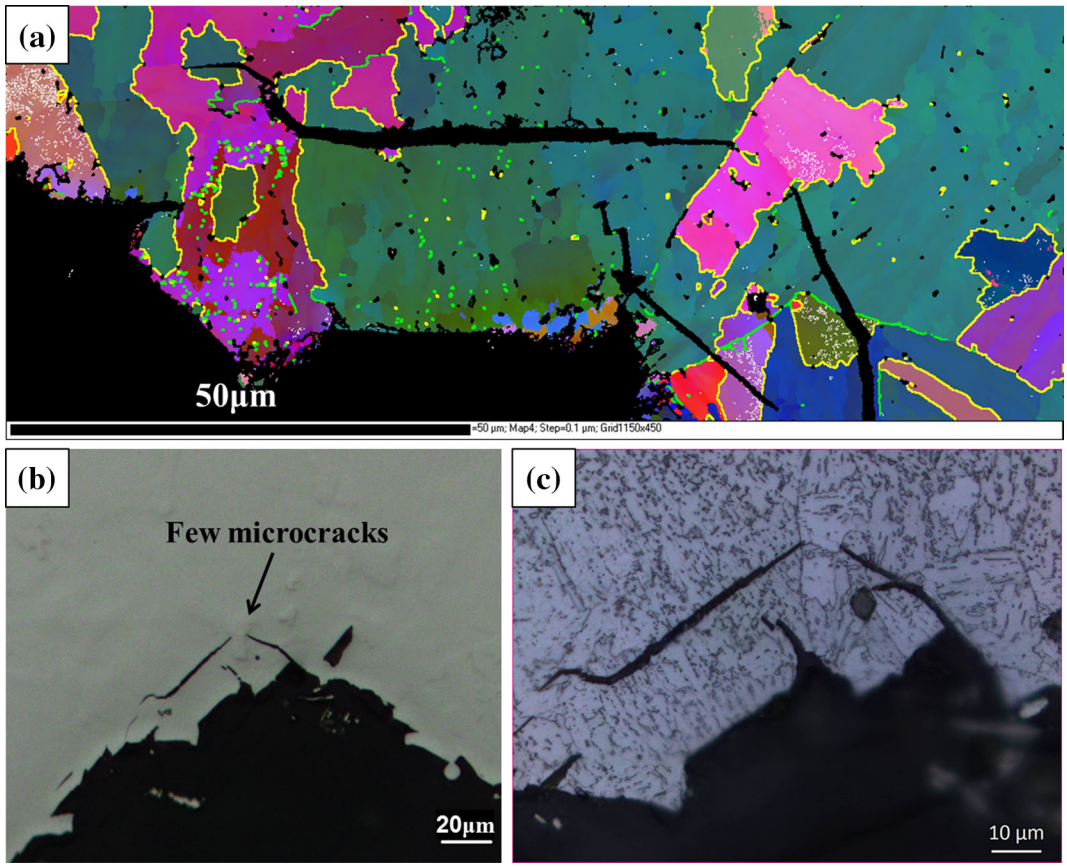

Fig. 7—Secondary microcracks underneath the CGHAZ (plane 1 of the sample with notch II) fracture surface. (*a*) EBSD all-Euler map (yellow line represents >45 deg grain boundary, green line represents 15-45 deg grain boundary); (*b*) LM micrograph of sample surface before EBSD scanning; (*c*) *In situ* metallograph of EBSD scanning area.

some instances, HAB can arrest the brittle cracks. For example, the longest crack in Figure 7(a) was arrested by the small pink grain. But the microstructure of CGHAZ and ICCGHAZ was primarily composed of granular bainite or upper bainite with low density of HAB which means low ability to arrest brittle cracks. Meanwhile, in the ICCGHAZ, majority of the grain boundaries were decorated by necklace-type M-A constituent, which makes the grain boundary weak. If the grain boundary is clean, crack nucleates through dislocation pile-up mechanism.[9,23] When necklace-type M-A constituent is present, cracking of M-A or debonding of M-A from matrix is the most probable crack initiation mechanism.[5–7] Figures 8(c) through (d) provided some side-evidence on cracking or debonding mechanism, although it is not clear enough. Strong evidence needs to be found in the future research.

IV. CONCLUSIONS

The microstructure of the ICCGHAZ consisted of granular bainite and upper bainite with necklace-type M−A constituent distributing along prior austenite grain boundaries. And the ICCGHAZ region played a dominant role in influencing the fracture behavior and impact energy. Low toughness of ~50 J was obtained when the notch encountered the ICCGHAZ region and high toughness of ~180 J when the notch did not contain the ICCGHAZ region. ICCGHAZ was found to be both the initiation site of the whole fracture and cleavage facet initiation site during brittle fracture propagation stage. The presence of necklace-type M-A constituent notably increased the susceptibility of cleavage microcrack nucleation. The study of secondary microcracks beneath the CGHAZ and the ICCGHAZ suggested that the fracture mechanism changes from nucleation-controlled in the CGHAZ to propagation-controlled in the ICCGHAZ. Both fracture mechanisms contribute to the low toughness of the sample contained ICCGHAZ.

ACKNOWLEDGMENTS

The authors acknowledge financial support from CBMM, CITIC Metal Co. Ltd., and National Basic Research Program of China (973 program, contract No. 2010CB630801). Thanks are due to China Scholarship Council (CSC) for the award of a scholarship

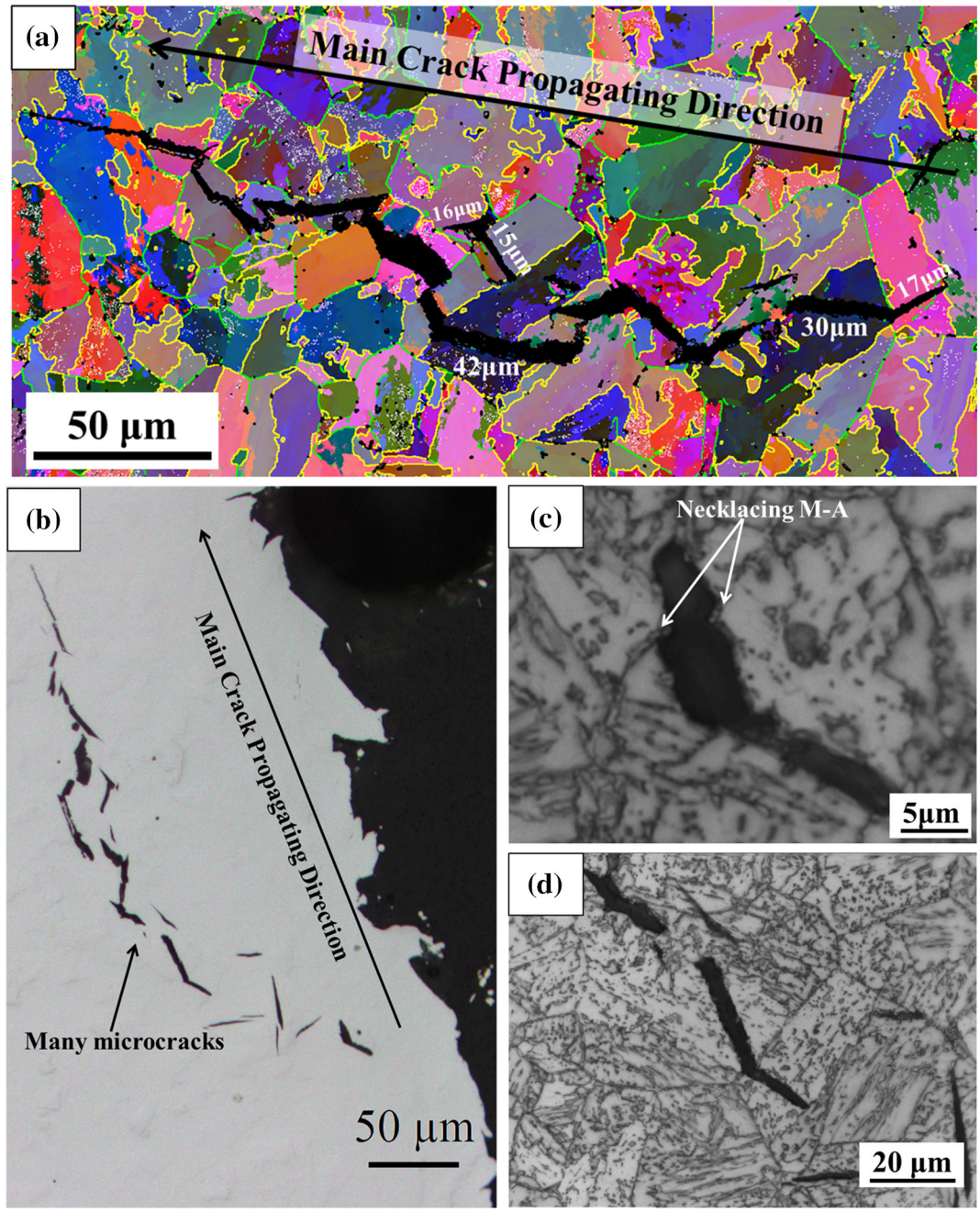

Fig. 8—Secondary microcracks underneath the ICCGHAZ (plane 2 of the sample with notch II) fracture surface. (*a*) EBSD all-Euler map (yellow line represents >45 deg grain boundary, green line represents 15-45 deg grain boundary); (*b*) LM micrograph of sample surface before EBSD scanning; (*c*) and (*d*) Metallographs of EBSD scanning area.

to Xueda Li for his research at McMaster University. We thank Glynis de Silveira, Andrei Carmen, and Chris Butcher in Canadian Centre for Electron Microscopy (CCEM) for the technical support.

REFERENCES

1. C.J. Shang, X.X. Wang, Q.Y. Liu, and J.Y. Fu: *Proceedings of the International Seminar on Welding of High Strength Pipeline Steel*, TMS, Araxa, Brazil, 2011, pp. 435–53.
2. C.J. Shang, X.D. Li, W.J. Nie, D.X. Xia, and S.J. Wu: *Proceedings of Recent Developments in High Strength Steels for Energy Applications*, MS&T, Pittsburgh, 2012.
3. F. Matsuda, Y. Fukada, H. Okada, C. Shiga, K. Ikeuchi, Y. Horii, T. Shiwaku, and S. Suzuki: *Weld. World*, 1996, vol. 37, pp. 134–54.
4. D.P. Fairchild: in *Welding Metallurgy of Structural Steels*, J.Y. Koo, ed., TMS-AIME, Warrendale, 1987, pp. 303–18.
5. C.L. Davis and J.E. King: *Metall. Mater. Trans. A*, 1994, vol. 25A, pp. 563–73.
6. P. Mohseni, J.K. Solberg, M. Karlsen, O.M. Akselsen, and E. Østby: *Metall. Mater. Trans. A*, 2014, vol. 45A, pp. 384–94.
7. Y. Li and T.N. Baker: *Mater. Sci. Technol.*, 2010, vol. 26, pp. 1029–40.

8. J.H. Chen, Y. Kikuta, T. Araki, M. Yoneda, and Y. Matsuda: *Acta. Metall.*, 1984, vol. 32, pp. 1779–88.
9. A.W. Thompson and J.F. Knott: *Metall. Trans. A*, 1993, vol. 24A, pp. 523–34.
10. D.A. Curry: *Met. Sci.*, 1980, vol. 14, pp. 319–26.
11. D.P. Fairchild, D.G. Howden, and W.A.T. Clark: *Metall. Mater. Trans. A*, 2000, vol. 31A, pp. 641–52.
12. R.O. Ritchie, J.F. Knott, and J.R. Rice: *J. Mech. Phys. Solids*, 1973, vol. 21, pp. 395–410.
13. J.R. Griffiths and D.R.J. Owen: *J. Mech. Phys. Solids*, 1971, vol. 19, pp. 419–31.
14. E. Bouyne, H.M. Flower, T.C. Lindley, and A. Pineau: *Scripta Mater.*, 1998, vol. 39, pp. 295–300.
15. T. Lin, A.G. Evans, and R.O. Ritchie: *Acta Metall.*, 1986, vol. 34, pp. 2205–16.
16. A. Lambert-Perlade, A.F. Gourgues, J. Besson, T. Sturel, and A. Pineau: *Metall. Mater. Trans. A*, 2004, vol. 35A, pp. 1039–53.
17. A.M. Guo, R.D.K. Misra, J.B. Liu, L. Chen, X.L. He, and S.J. Jansto: *Mater. Sci. Eng. A*, 2010, vol. 527, pp. 6440–48.
18. J. Nohava, P. Hausild, M. Karlik, and P. Bompard: *Mater. Charact.*, 2003, vol. 49, pp. 211–17.
19. V. Venegas, F. Caleyo, J.L. Gonzalez, T. Baudin, J.M. Hallen, and R. Penelle: *Scripta Mater.*, 2005, vol. 52, pp. 147–52.
20. H.G. Jian, F. Jiang, L.L. Wei, X.Y. Zheng, and K. Wen: *Mater. Sci. Eng. A*, 2010, vol. 527, pp. 5879–82.
21. X.D. Li, X.P. Ma, S.V. Subramanian, C.J. Shang, and R.D.K. Misra: *Mater. Sci. Eng. A*, 2014, vol. 616, pp. 141–47.
22. Y. You, C.J. Shang, W.J. Nie, and S. Subramanian: *Mater. Sci. Eng. A*, 2012, vol. 558, pp. 692–701.
23. A. Pineau: *Int. J. Fract.*, 2006, vol. 138, pp. 139–66.